

## Article

# Mg–Fe Layered Double Hydroxides/Polyacrylonitrile Nanofibers for Solar-Light Induced Peroxymonosulfate Elimination of Tetracycline Hydrochloride

Hao Peng <sup>1,\*</sup> , Beilei Ye <sup>2</sup>, Meiying Luo <sup>2</sup> and Xiaogang Zheng <sup>2,\*</sup><sup>1</sup> College of Chemistry and Chemical Engineering, Yangtze Normal University, Chongqing 408100, China<sup>2</sup> College of Chemistry and Chemical Engineering, Neijiang Normal University, Neijiang 641100, China

\* Correspondence: cqupenghao@126.com (H.P.); zhengxg123456@163.com (X.Z.)

**Abstract:** The photo-induced peroxymonosulfate (photo-PMS) reaction is a promising route to eliminate antibiotics from waste water. To achieve excellent photo-PMS activity in Mg–Fe layered double hydroxides (LDHs) for tetracycline hydrochloride (TCH) degradation under simulative solar-light irradiation, Mg–Fe LDHs-loaded polyacrylonitrile (Mg–Fe/PAN) nanofibers were in-situ prepared via the hydrothermal route. For comparison to the photocatalysis and photo-PMS process, the Mg–Fe/PAN-assisted photo-PMS process exhibited a better elimination activity for TCH elimination. In addition, the photo-PMS activities of Mg–Fe/PAN composites were greatly affected by Mg–Fe LDHs content, TCH concentration, pH, and inorganic salts. Among these Mg–Fe/PAN composites, the optimal MgFe<sub>2</sub>/PAN with a Mg/Fe molar ratio of 1:2 and a nominal Mg–Fe LDHs content of 2.0 wt. % removed 81.31% TCH solution of 80 mg L<sup>-1</sup> TCH within 120 min. This enhanced photo-PMS capacity of MgFe<sub>2</sub>/PAN was ascribed to the abundant active sites formed by functional groups and oxygen defects for efficient TCH species adsorption and photon capturing, and the tight interface between Mg–Fe LDHs nanoparticles and PAN nanofibers for the rapid separation and transfer of photoinduced e<sup>-</sup>/h<sup>+</sup> pairs. SO<sub>4</sub><sup>•-</sup> and •O<sub>2</sub><sup>-</sup> radicals were vital for the MgFe<sub>2</sub>/PAN-assisted photo-PMS reaction.

**Keywords:** Mg–Fe LDHs; PAN nanofibers; solar light; photo-peroxymonosulfate

**Citation:** Peng, H.; Ye, B.; Luo, M.; Zheng, X. Mg–Fe Layered Double Hydroxides/Polyacrylonitrile Nanofibers for Solar-Light Induced Peroxymonosulfate Elimination of Tetracycline Hydrochloride. *Water* **2024**, *16*, 1345. <https://doi.org/10.3390/w16101345>

Academic Editor: Anastasios Zouboulis

Received: 9 April 2024

Revised: 6 May 2024

Accepted: 7 May 2024

Published: 8 May 2024



**Copyright:** © 2024 by the authors. Licensee MDPI, Basel, Switzerland. This article is an open access article distributed under the terms and conditions of the Creative Commons Attribution (CC BY) license (<https://creativecommons.org/licenses/by/4.0/>).

## 1. Introduction

As common pharmaceuticals used against the numerous disease-causing bacteria in animals and humans, tetracyclines (TCs) are the second-most intensively used antibiotics due to their specific capacities, such as anticancer, proteolysis, angiogenesis, anti-inflammation, bone-metabolism, anti-apoptosis, and metal ions chelation [1–3]. TCs are composed of phenolic hydroxyl groups, acylamino groups, dimethylamino moieties, and ketone-enol double bonds. The low Henry constants varied from  $3.45 \times 10^{-24}$  to  $3.91 \times 10^{-26} \text{ atm}^3 \text{ mol}^{-1}$ , inducing stable and high resistance to oxidation. Due to the high consumption rate and the low metabolism, 60~90% TCs and their metabolized forms are not used in living organisms, and are further released into environment via feces and urine, causing the serious scarcity of water sources [4,5]. What is worse, the long-term exposure to TCs induces chronic and even acute disease, endangering humans and the ecosystem [6]. To overcome the harmful impacts of TCs in water, various strategies have been explored in previous works, including adsorption [7,8], advanced oxidation [9,10], biodegradation [11,12], electrocatalysis [13,14], photocatalysis [15,16], filtration [17], and flocculation [18]. Among these approaches, photocatalysis is the most promising route to eliminate TCs through the conversion of solar light to chemical and thermal energies. The key issue met in using this technology is fabricating novel photocatalysts with excellent photo-activity and easy recyclability.

To date, inorganic and organic semiconductors have been explored to enhance the conversion efficiency of solar light in photocatalytic system [19]. Among the reported pho-

photocatalysts, metal oxides and metal sulfides are intensively investigated due to their ideal band-gap structure for charge separation and migration. Different from metal oxides and metal sulfides, layered double hydroxide (LDH) is a typical ionic layer composite consisting of metal cations and hydroxyl groups [20]. LDH is defined as  $[M^{2+}_{1-x}M^{3+}_x(OH)_2]^{x+}A^{m-}_{x/m} \cdot nH_2O$ , of which M and A are the metal cation in the terrace and the compensative anion in the interlayer, respectively. Owing to the oxo bridge and semiconductor metal element in the layered structure used for the efficient electron transfer, LDHs with charge neutrality and a stabilized structure have drawn great attention in relation to adsorption and photocatalysis [21,22]. Considering that LDHs exhibit weak visible light absorption and serious recombinations of photo-induced  $e^-/h^+$  pairs, LDHs coupled with semiconductors such as CuFe LDH/ $Bi_2WO_6$  [23], CuFe-LDH/ $TiO_2$  [24], FeNi-LDH/ $Ti_3C_2$  [25], CuMgFe-B(OH) $_4$  LDH [26],  $Bi_2WO_6/CoAl$ -LDH [27], and  $MoO_2@CoFe$  LDH [28] have been confirmed as the most efficient catalysts in photo-Fenton reactions. This is ascribed to the strong Fe(III)/Fe(II) redox cycles for efficient electron scavengers and the internal electric field of the heterojunction structure for rapid  $e^-/h^+$  separation and conversion into  $\bullet OH$  radicals. For comparison to the reported Fe-based LDHs, the higher surface reactivity and iron redox cycling of Mg-Fe LDH are much more favorable for generating  $\bullet OH$  and  $\bullet O_2^-$  [29]. In the Fenton system,  $Fe^{2+}$  ions react with  $H_2O_2$  to form  $Fe^{3+}$ ,  $\bullet OH$  and  $OH^-$ , and then  $H_2O_2$  reacts with  $\bullet OH$  to generate  $H_2O$  and  $\bullet OOH$ , and further,  $Fe^{3+}$  reacts with  $\bullet OOH$  to obtain  $Fe^{2+}$ ,  $H_2$  and  $O_2$  [30]. Meanwhile, the dissolved  $O_2$  is efficiently consumed by  $e^-$  to form  $\bullet O_2^-$ . The surface -OH groups of Mg-Fe LDHs favor the adsorption of organic pollutants via the hydrogen-bonding force, meanwhile facilitating the formation of active radicals via efficient photon capture, leading to their excellent photo-Fenton activity. However, the pristine LDHs suffer from poor compatibility between the super redox ability and efficient visible light absorption.

Although massive efforts have focused on the enhancement of active sites, radical generation, and electron transfer rates to address the above disadvantage and to enlarge the photocatalytic efficiency of LDHs via structure tuning, heteroatoms doping, heterojunction constructing, and oxygen defects, how to recycle LDH bulks from wastewater is scarcely discussed in previous works [31,32]. In recent years, nanoparticle pollution has become a serious and dangerous form of pollution due to its small size, which easily penetrates animal and plant cells. Nanoparticles can easily migrate from water to soil and float into air, and further accumulate from plants and animals into humans to cause deleterious effects [33]. In addition, their high surface energy leads to the aggregation of photocatalyst nanoparticles in aqueous solution, and inferior separation efficiency after photocatalytic reaction. Therefore, the excellent dispersion of nanosized photocatalysts on the appropriate carriers is a promising route to address the above matters. Owing to their super hydrophobicity and micropore structure that contribute to the efficient separation of nanomaterials, their large surface-to-volume ratios for abundant loading sites, and their small density for sufficient exposure to light, polyacrylonitrile (PAN) nanofibers have drawn intensive attention as supporters of photocatalysts [34]. PAN nanofibers-based photocatalysts are fabricated to enhance the amounts of photon-capturing sites, and to form tight junction interfaces for the rapid separation and transfer of  $e^-/h^+$  pairs, including CdS-BiOCl/PAN [35], g- $C_3N_4$ /PAN/PANI@ $LaFeO_3$  [36], PAN/ $TiO_2$  [37],  $Bi_2O_2CO_3/g-C_3N_4@PAN$  [38], PAN/ $BiInOCl$  [39], PAN- $Bi_2O_2CO_3-BiOI$  [40],  $SrTiO_3/PAN/FLG$  [41], and  $Bi_2MoO_6/S-C_3N_4/PAN$  [42]. To the best of our knowledge, Mg-Fe LDH combined with PAN has been not fabricated to boost photocatalytic activity and durability via TCs elimination. There are no works on the charge transfer mechanisms of photoinduced  $e^-/h^+$  pairs between Mg-Fe LDH and PAN nanofibers for the photo-PMS degradation of pollutants from wastewater.

Herein, Mg-Fe LDH nanoparticles were in-situ loaded onto the surface of PAN (Mg-Fe/PAN) nanofibers via the hydrothermal route for evaluating the solar-light activated persulfate oxidation of TCH. In comparison to the  $\bullet OH$  and  $\bullet O_2^-$  radicals formed in a photocatalytic or Fenton system, the sulfate radical ( $SO_4^{\bullet-}$ ) generated in persulfate-based

oxidation reactions has a higher redox potential, better selectivity, and longer half-life, thus gaining greater destructiveness in the internal structure of TCH molecules [43]. Differently from the addition of Mg–Fe LDH into a PAN solution to electrospin Mg–Fe/PAN nanofibers, Mg–Fe LDH nanoparticles were in-situ grown on the skeleton of PAN nanofibers to avoid the coverage of the active surface and the reduction in mechanical stability. In addition, Mg–Fe/PAN nanofibers were used as the three-dimensional porous membrane photocatalyst with high specific surface area, superior light absorption ability, and excellent hydrophilicity [44]. The syngenetic effects of bimetallic Mg–Fe LDH in the orderly laminar and spatial structure are favorable for the solar-light induced activation of peroxymonosulfate (PMS). In addition, PAN nanofibers were likely to restrain the agglomeration of Mg–Fe LDH, enlarging the photo-PMS activity and stability for TCH elimination.

## 2. Experimental

### 2.1. Preparation of Mg–Fe/PAN Nanofibers

Mg–Fe/PAN nanofibers were fabricated via the hydrothermal route. Firstly, 1.00 g polyacrylonitrile ((C<sub>3</sub>H<sub>3</sub>N)<sub>n</sub>, Mw = 150,000) was dissolved into 20 mL N,N-Dimethylformamide HCON(CH<sub>3</sub>)<sub>2</sub> under intensive stirring for 1.0 h at 353 K. Then, the above solution was transferred to a spinning reactor operated at 22 kV, and the spinning rate of  $2.0 \times 10^{-6} \text{ m s}^{-1}$  was set to obtain PAN nanofibers. Mg–Fe/PAN with a Mg/Fe molar ratio of 1:2 and a nominal Mg–Fe LDH content of 2.0 wt. % was prepared as follows: 0.085 g FeCl<sub>3</sub>·6H<sub>2</sub>O, 0.074 g Mg(NO<sub>3</sub>)<sub>2</sub>·6H<sub>2</sub>O, 0.10 g PAN nanofibers, and 1.50 g urea (CO(NH<sub>2</sub>)<sub>2</sub>) were added to 30 mL deionized water, stirred at room temperature for 30 min, poured into a 50 mL reactor, treated at 433 K for 16 h, washed with deionized water three times, and dried at 353 K to obtain MgFe<sub>2</sub>/PAN. Based on the above process, MgFe/PAN, MgFe<sub>3</sub>/PAN and Mg<sub>2</sub>Fe/PAN were prepared with Mg/Fe molar ratios of 1:1, 1:3, and 2:1, respectively. These Mg–Fe/PAN samples had a nominal Mg–Fe LDHs content of 2.0 wt. %. Mg(OH)<sub>2</sub>/PAN with a Mg(OH)<sub>2</sub> content of 2.0 wt. % and Fe(OH)<sub>3</sub>/PAN with an Fe(OH)<sub>3</sub> content of 2.0 wt. % were also fabricated using NH<sub>3</sub>·H<sub>2</sub>O for the comparative investigation. These samples were evaluated via the various characterization methods (Supported Information S1).

### 2.2. Photo-PMSTesting

Photo-PMS performances of Mg–Fe/PAN nanofibers in TCH elimination were assessed with a Xe lamp with a power intensity of 300 mW cm<sup>-2</sup>, an irradiated distance of 20 cm, and a 420 nm cutoff filter. Briefly, 40 mg MgFe/PAN bulks were dispersed into 150 mL TCH solution of 80 mg L<sup>-1</sup>, and stirred in the dark at room temperature for 60 min. After attaching the adsorption–desorption balance, 0.1 g potassium peroxymonosulfate (KHSO<sub>5</sub>) bulks were added to the above solution with intensive stirring. Then, 2 mL solution was sampled, filtered, and analyzed by high-performance liquid chromatography (Agilent 1260II, Tokyo, Japan) at a specific interval of 10 min. The effects of TCH concentration, Mg/Fe molar ratio, inorganic salts, pH, and quenchers on the photo-PMS performances of Mg–Fe/PAN hybrids on TCH removal were well investigated. The used samples were washed with 50 mL deionized water three times under an intensive ultrasound treatment, and dried at 353 K for 6 h for the next cycle of testing. The reproducibility of photo-PMS testing was assessed three times, with an error range of ±3%.

## 3. Results and Discussion

### 3.1. Characterization

Electrostatic spinning was a promising route to fabricate PAN nanofibers with a diameter of around 100 nm (Figure 1A,B). PAN nanofibers easily formed into a PAN mat in the electrostatic spinning process, and further served as the support for nanoparticles. Owing to the sufficient N–H bonds of PAN nanofibers, 100 nm Fe(OH)<sub>3</sub> nanoparticles (Figure 1C,D) were efficiently bonded on the surfaces of PAN nanofibers via the H-bond effect, which was also confirmed by Mg(OH)<sub>2</sub>/PAN with around 50 nm Mg(OH)<sub>2</sub> nanoparticles (Figure 1E,F) and Mg–Fe/PAN composites with about 50 nm Mg–Fe LDHs nanoparticles. For compar-

ison, Mg–Fe/PAN with various Mg/Fe molar ratios had smaller Mg–Fe nanoparticles loaded on the PAN surface (Figure S1); 40 nm Mg–Al LDHs nanoparticles were loaded onto the surface of PAN nanofibers to form MgFe<sub>2</sub>/PAN (Figure 1G,H), which had more Mg–Al nanoparticles than MgFe<sub>3</sub>/PAN (Figure S1E,F). Elemental mapping images (Figure S2) suggest that Mg, Fe, O, C, and N elements appeared on the MgFe<sub>2</sub>/PAN, which was further confirmed by the EDX pattern.

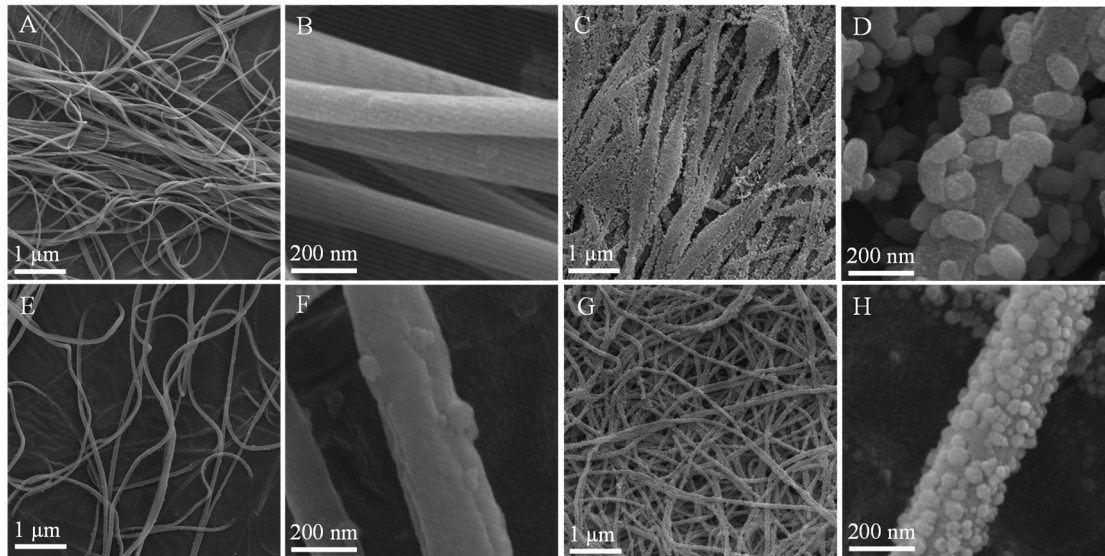


**Figure 1.** SEM images of PAN nanofibers (A,B), Fe(OH)<sub>3</sub>/PAN (C,D), Mg(OH)<sub>2</sub>/PAN (E,F), and MgFe<sub>2</sub>/PAN (G,H).

The Mg/Fe molar ratio slightly changed the mass contents of Mg and Fe in Mg–Fe/PAN composites (Table S1), while it affected the valence states of surface compositions. For MgFe<sub>2</sub>/PAN, the (010) plane of the PAN phase (JCPDS, 48-2119) and (004) facet of the Mg–Fe LDH phase (JCPDS, 14-0365) appeared at 16.69° and 21.16°, respectively (Figure 2A). Due to the small Mg–Fe LDHs content and poor lattice structure, the diffraction peaks of Mg–Fe LDHs phases were not obviously detectable in the XRD pattern. Mg, Fe, C, N, and O elements were well detected in the MgFe<sub>2</sub>/PAN composite. The Mg 1s peak was located at 1305.83 eV (Figure 2B). The divided Fe 2p peaks at 721.34 and 708.24 eV were assigned to Fe 2p<sub>1/2</sub> and Fe 2p<sub>3/2</sub>, and the peaks at 723.18 and 712.93 eV were indexed as the corresponding shake-up satellites, respectively (Figure 2C). Considering the binding energy of additional carbon located at 283.95 ± 0.5 eV, the C 1s peaks at 285.11, 283.66, and 282.31 eV (Figure 2D) were indexed as C≡N, C–C, and C–H bonds of the PAN compound, respectively [45,46]. The split N 1s peaks at 397.76 and 396.44 eV (Figure 2E) were indexed as C≡N and N–H bonds, respectively. Considering that Mg–Fe LDH consisted of Mg<sub>1-x</sub>Fe<sub>x</sub>(OH)<sub>2</sub>CO<sub>3</sub>)<sub>x/2</sub>·nH<sub>2</sub>O, O 1s peaks at 530.22, 528.85, and 527.54 eV (Figure 2F) were indexed as oxygen vacancies/defects, oxygen lattices of Mg–O/Fe–O bonds, and oxygen species of the CO<sub>3</sub><sup>2-</sup> group, respectively [47]. These functional groups of MgFe<sub>2</sub>/PAN as well as oxygen vacancies served as the vacant sites of TCH adsorption and photon capture, especially the junction sites formed between Mg–Fe LDH and PAN nanofibers for boosting the charge transfer and separation.

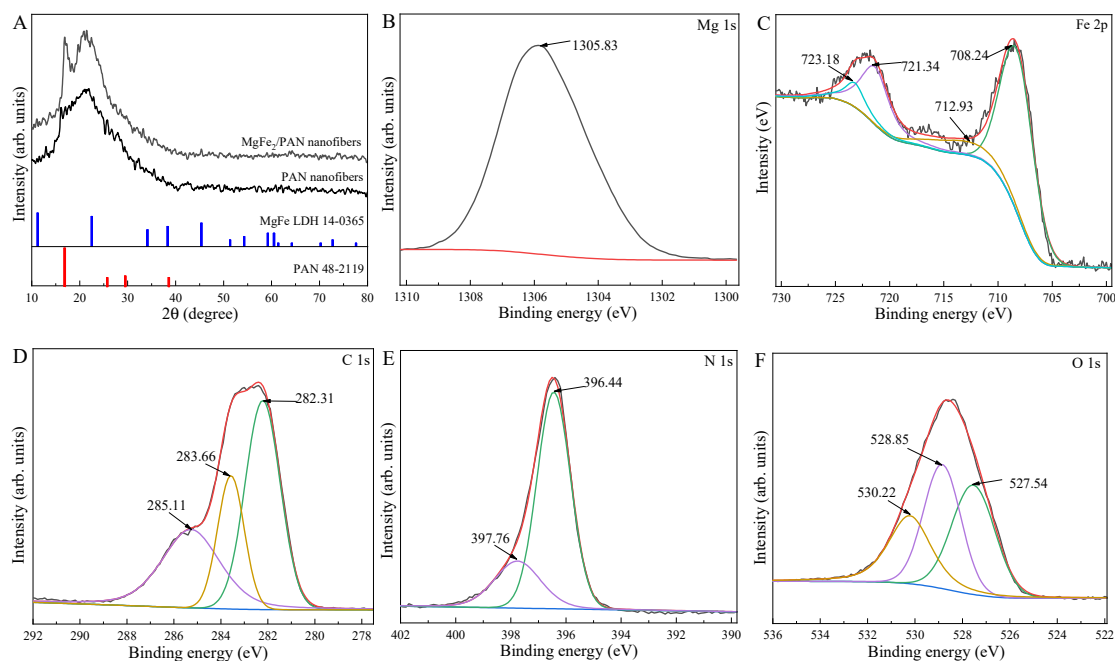


**Figure 2.** XRD pattern (A), XPS spectra of Mg 1s (B), Fe 2p (C), C 1s (D), N 1s (E), and O 1s (F) of MgFe<sub>2</sub>/PAN.

The UV-Vis DRS curves (Figure 3A) suggest that PAN nanofibers and Mg(OH)<sub>2</sub>/PAN only had a UV light absorption capacity, while Fe(OH)<sub>3</sub>/PAN and MgFe<sub>2</sub>/PAN extended the light absorption edge to the visible light region. Mg-Fe/PAN composites with various Mg/Fe molar ratios (Figure S3A) also had a strong visible light response, meaning better solar light utilization. Based on the plots of  $(\alpha h\nu)^{1/2}$  vs.  $(h\nu)$  (Figure 3B), the estimated band-gap energy ( $E_g$ ) values of PAN nanofiber, and Mg(OH)<sub>2</sub>/PAN, Fe(OH)<sub>3</sub>/PAN, and MgFe<sub>2</sub>/PAN samples (Table S1), were 3.84, 2.83, 1.75, and 1.67 eV, respectively. For comparison, MgFe<sub>2</sub>/PAN has a narrower band-gap structure. Of course, Mg/Fe molar ratios affected the  $E_g$  values of Mg-Fe/PAN samples (Figure S3B) due to the changes in oxygen vacancies in the surroundings of Fe-O and Mg-O bonds. Considering that the tangent slopes of Mott-Schottky plots (Figures 3C and S3C) were positive, Mg(OH)<sub>2</sub>/PAN, Fe(OH)<sub>3</sub>/PAN, and Mg-Fe/PAN composites were n-type materials. The flat band potential ( $E_{FB}$ ) of MgFe<sub>2</sub>/PAN (Table S1) was  $-1.03$  V, and its conduction band energy ( $E_{CB}$ ) was  $-0.83$  eV. Hence, the valance band energy ( $E_{VB}$ ) of MgFe<sub>2</sub>/PAN was 0.84 eV. The electrochemical impedance spectra and PL were indicators for the separation and recombination of photo-excited  $e^-/h^+$  pairs. Among these PAN-based composites, MgFe<sub>2</sub>/PAN had the smallest circular arc radius of electrochemical impedance spectra (Figure 3D) and the weakest PL intensity (Figure 3F). It is indicated that the combined effects of Mg-Fe LDH and PAN nanofibers were favorable for the separation and transfer of charge carriers. This was further confirmed by Mg-Fe/PAN composites with the various molar ratios of Mg/Fe in LDHs (Figure S3D). In contrast with PAN nanofibers, Mg(OH)<sub>2</sub>/PAN, and Fe(OH)<sub>3</sub>/PAN and MgFe<sub>2</sub>/PAN composites (Figure 3E), had stronger photocurrents, while the photocurrent intensity was not stable because of the lattice defects formed in MgFe<sub>2</sub>/PAN composites, such as oxygen vacancies. It is indicated that MgFe<sub>2</sub>/PAN had the stronger solar light utilization capacity, while its separation efficiency of photo-excited  $h^+/e^-$  pairs in each “on-off” cycle was not satisfactory. When the light was turned on, MgFe<sub>2</sub>/PAN rapidly absorbed the light to form a photocurrent, and further increased with the increasing irradiation time. When the light was turned off, the generated electron-holes pairs were not efficiently quenched, decreasing the photocurrent. The declining photocurrent intensity induced a weak photocatalytic activity of Mg-Fe/PAN in the photocatalytic system. Of course, the adsorption activity of Mg-Fe/PAN greatly affected the photo-PMS

activity. The adsorption capacities of the obtained samples were related to the functional groups and surface discharge. As shown in the FT-IR spectrum (Figure S4), PAN nanofibers exhibited functional groups such as  $C\equiv N$  and  $C=C$  bonds, which were favorable for connecting Mg-Fe LDHs to generate much more groups, such as N-H, O-H, and Mg-O-Fe. The Zeta potential curve (Figure S5) suggests that the isopotential point of  $MgFe_2/PAN$  was  $pH = 3.92$ . In other words,  $MgFe_2/PAN$  exhibited a surface positive charge at  $pH < 3.92$ , while the surface negative charge was  $pH > 3.92$ . This special surface charge nature of  $MgFe_2/PAN$  was responsible for its photo-PMS performance in TCH removal.

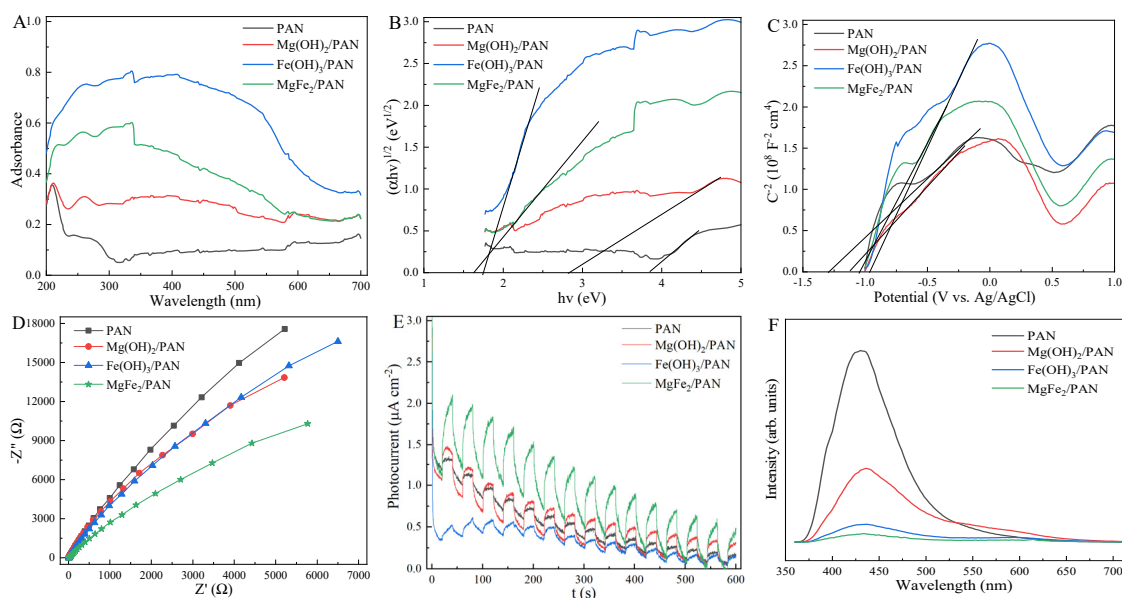


**Figure 3.** UV-Vis DRS curves (A), plots of  $(h\nu)$  versus  $(\alpha h\nu)^{1/2}$  (B), Mott-Schottky curves (C), electrochemical impedance spectra (D), photocurrent curves (E), and PL spectra (F) of PAN-based samples.

### 3.2. Photo-PMS Performance

The catalytic activities of PAN-based samples were analyzed by the photo-PMS elimination of TCH solution, which consisted of adsorption and photo-PMS efficiencies. The intermediate types generated in the photo-PMS system were greatly affected by the conditions and photocatalyst types. It is difficult to check the possible intermediates in a photo-PMS system, and the most efficient route is to analyze the removal efficiency of TCH in aqueous solution. As plotted in Figure 4A, the removal efficiency as well as adsorption and photo-PMS efficiencies of  $MgFe_2/PAN$  were higher than those of PAN,  $Mg(OH)_2/PAN$ , and  $Fe(OH)_3/PAN$ . It is indicated that the elimination efficiency of TCH over PAN could be enhanced by  $Mg(OH)_2$ ,  $Fe(OH)_3$ , and Mg-Fe LDH due to the functional groups, such as N-H and O-H bonds, as well as oxygen vacancies acting as the adsorption and photocatalysis sites. The removal efficiency of  $MgFe_2/PAN$  with a Mg/Fe molar ratio of 1:1 was higher than that of  $Mg_2Fe/PAN$  with a Mg/Fe molar ratio of 2:1, while it was lower than  $MgFe_2/PAN$  with a Mg/Fe molar ratio of 1:2 for the photo-PMS elimination of TCH. The best removal efficiency over optimal  $MgFe_2/PAN$  was 81.31% after 120 min. To further explain the merit of photo-PMS reaction over  $MgFe_2/PAN$ , a comparative investigation was carried out for the degradation of  $80 mg L^{-1}$  TCH solution. As shown in Figure 4B, the photo-PMS efficiency without  $MgFe_2/PAN$  was 47.24%, the photocatalytic efficiency over  $MgFe_2/PAN$  was 23.65%, while the photo-PMS efficiency over  $MgFe_2/PAN$  was 81.31%. It is confirmed that the combined effect of photo-PMS over  $MgFe_2/PAN$  was better than the sum of photocatalysis and PMS. The separated electrons and holes over  $MgFe_2/PAN$  favored the formation of radicals, and these radicals were further likely to excite the Fe(II)/Fe(III) couple and PMS species to convert TCH species into harmless

products. In comparison to the previous works on the photocatalysis, photo-Fenton, and photo-persulfate degradation of TCH solution (Table S2), here, the photo-PMS reaction had a better removal capacity than  $\text{MgFe}_2/\text{PAN}$ . It is indicated that  $\text{MgFe}_2/\text{PAN}$  was the potential catalyst for the photo-PMS elimination of antibiotics from wastewater. Of course, the photo-PMS reaction was intensively affected by TCH concentration, pH, and inorganic salts.

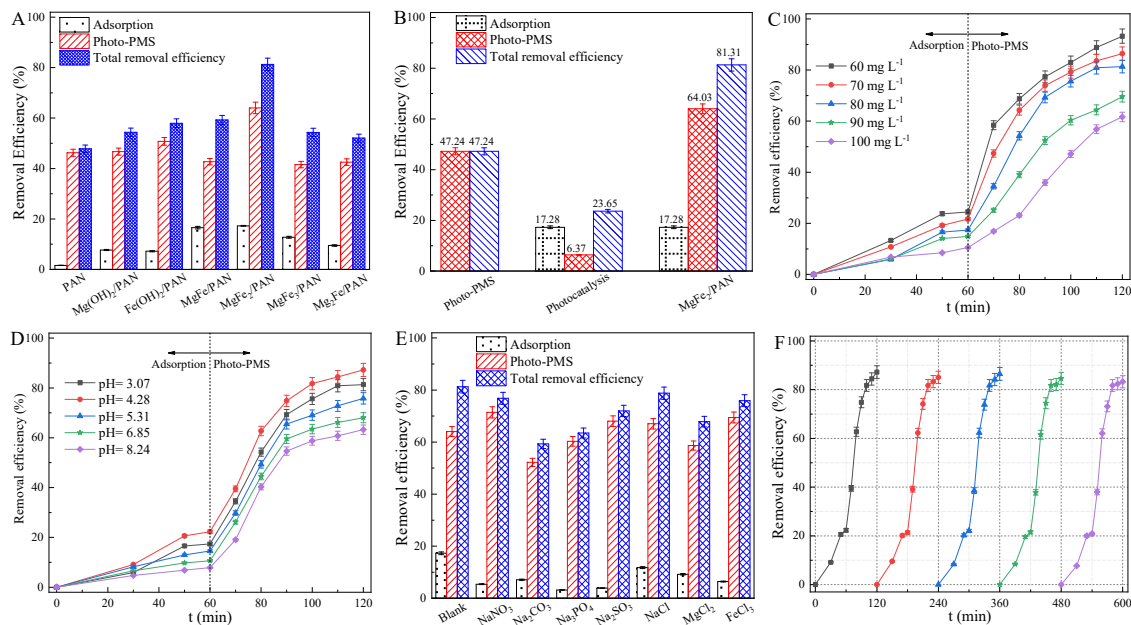


**Figure 4.** Photo-PMS performances of PAN-based samples in TCH removal (A), comparative investigation of photo-PMS behaviors in different conditions (B), effects of TCH concentration (C), pH (D), and inorganic salts (E) on the photo-PMS activity of  $\text{MgFe}_2/\text{PAN}$  and the photo-PMS durability of  $\text{MgFe}_2/\text{PAN}$  (F).

When the TCH solution ranged from 60 to  $100 \text{ mg L}^{-1}$  (Figure 4C), the adsorption and photo-PMS activity over  $\text{MgFe}_2/\text{PAN}$  declined from 93.24% to 61.63% under the same conditions. The main reason was the limitation of active sites for adsorption and photon conversion. Based on the plots of  $-\ln(C_t/C_0)$  versus  $t$ , the kinetic constant of  $\text{MgFe}_2/\text{PAN}$  decreased with the increasing TCH concentration (Figure S6), meaning the fast conversion of TCH over  $\text{MgFe}_2/\text{PAN}$  at the low TCH concentration. Although the high TCH concentration provided mass transfer for TCH adsorption at vacant sites, it also served to induce mass transfer resistance that hindered the escape of photo-PMS products from active sites [48,49]. In addition, the high TCH content in the aqueous solution was not favorable for the photon capture over active sites and the transfer and separation of photo-excited  $e^-/h^+$  pairs at the junction interface [47,50]. There were abundant  $\text{OH}^-$  and  $\text{CO}_3^{2-}$  ions formed in  $\text{MgFe}_2$  LDH, which favored the adsorption of cationic and zwitterionic TCH species. Due to the various TCH species that emerged under different pH conditions, we can infer that pH greatly affected the adsorption and photo-PMS activities of  $\text{MgFe}_2/\text{PAN}$ . When pH increased from 3.07 to 8.24, the adsorption and photo-PMS efficiencies of  $\text{MgFe}_2/\text{PAN}$  climbed and then declined, and the best removal efficiency of TCH was observed at a pH of 4.28 (Figure 4D). A similar result was obtained in the kinetic constant of  $\text{MgFe}_2/\text{PAN}$  in the pH range of 3.07~8.24. The increasing pH induced the increase and then decline in the kinetic constant of  $\text{MgFe}_2/\text{PAN}$  (Figure S7). Of course, inorganic ions also affected the pH of the TCH solution, and could be competitively adsorbed at the vacant sites instead of TCH species, hindering the adsorption and photo-PMS capacities of  $\text{MgFe}_2/\text{PAN}$ . For example,  $\text{NaNO}_3$  and  $\text{NaCl}$  slightly suppressed, while  $\text{Na}_2\text{CO}_3$ ,  $\text{Na}_2\text{SO}_3$ , and  $\text{Na}_3\text{PO}_4$  seriously restrained, the removal efficiency of TCH (Figure 4E).  $\text{FeCl}_3$  seriously restrained

the adsorption capacity, while it enhanced the photo-PMS efficiency because of the redox of the Fe(II)/Fe(III) couple. Considering the complex composition of real wastewater, the obtained MgFe<sub>2</sub>/PAN was not applied in a scaled-up photocatalytic system for TCH elimination. Future work will focus on the industrial application of Mg-Fe/PAN composites in real wastewater.

### 3.3. Photo-PMS Durability

For the durability testing, the used MgFe<sub>2</sub>/PAN sample was washed with deionized water three times, and then used for the photo-PMS degradation of 70 mg L<sup>-1</sup> TCH solution. The removal efficiency of TCH over MgFe<sub>2</sub>/PAN (Figure 4F) decreased from 87.23% to 83.39% after five cycles. This deactivation of MgFe<sub>2</sub>/PAN was ascribed to the photo-corrosion under long-term irradiation, changing the valance states of compositions (Figure S4). In comparison to the fresh MgFe<sub>2</sub>/PAN, the Mg 1s peak of the sample used changed to 1304.12 eV (Figure S8A). The binding energies of Fe 2p<sub>1/2</sub>, Fe 2p<sub>3/2</sub>, and their corresponding satellite speaks shifted to 721.53, 708.23, 723.52, and 710.94 eV, respectively (Figure S8B). In contrast with fresh sample (13.10 eV), the larger spacing distances between the Fe 2p peaks in the used sample indicate the weaker electron intensity, which is thus not favorable for the redox reaction of Fe(II)/Fe(III) couples. The C 1s peaks of used sample belonging to C≡N, C–C, and C–H bonds of PAN (Figure S8C) changed to 285.11, 283.56, and 282.55 eV, respectively. The split O 1s peaks indexed as oxygen vacancies/defects, oxygen lattices of Mg–O/Fe–O bonds, and oxygen species of the CO<sub>3</sub><sup>2-</sup> group (Figure S8D), respectively, migrated to 530.65, 529.16, and 527.93 eV. Compared with fresh sample (397.76 eV, 396.44 eV), the N 1s peaks of the used sample, assigned to C≡N and N–H bonds (Figure S8E), shifted to 397.66 and 397.65 eV, respectively. However, the SEM images (Figure S9) confirm that the texture structure of the used MgFe<sub>2</sub>/PAN was not changed, implying the excellent textural stability of MgFe<sub>2</sub>/PAN.

### 3.4. Photo-PMS Mechanism

The photo-excited radicals of MgFe<sub>2</sub>/PAN in photo-PMS system were checked by the quenching test, including MeOH (SO<sub>4</sub><sup>•-</sup> and •OH), *p*-BQ (•O<sub>2</sub><sup>-</sup>), *t*-BuOH (•OH), L-Histidine (<sup>1</sup>O<sub>2</sub>), KBrO<sub>3</sub> (e<sup>-</sup>), and EDTA-2Na (h<sup>+</sup>). As plotted in Figure 5, MeOH and *p*-BQ seriously restrained the photo-PMS activity of MgFe<sub>2</sub>/PAN. The photo-PMS efficiencies of TCH over MgFe<sub>2</sub>/PAN with the addition of EDTA-2Na and *t*-BuOH were higher than those with the presence of MeOH, *p*-BQ, L-Histidine, and KBrO<sub>3</sub>. It is suggested that SO<sub>4</sub><sup>•-</sup> and •O<sub>2</sub><sup>-</sup> were vital, while •OH and h<sup>+</sup> were less important for MgFe<sub>2</sub>/PAN-assisted photo-PMS reaction. The possible photo-PMS mechanism of MgFe<sub>2</sub>/PAN was proposed in Figure 6. Mg-Fe LDHs nanoparticles were well loaded on the surface of PAN mats, of which the Mg-Fe LDH layers with oxygen vacancies were in good contact with CO<sub>3</sub><sup>2-</sup> ions. Considering that the E<sub>CB</sub> and E<sub>VB</sub> values of MgFe<sub>2</sub>/PAN were, respectively, -0.83 and 0.84 eV, we can infer that the photogenerated electrons migrated from the valance band to the conduction band, achieving the rapid separation and transfer of e<sup>-</sup>/h<sup>+</sup> pairs at the junction interface. Due to the more negative value of E<sub>CB</sub> than the potential value of O<sub>2</sub>/•O<sub>2</sub><sup>-</sup> (-0.33 eV), e<sup>-</sup> was efficiently consumed by dissolved O<sub>2</sub> to produce •O<sub>2</sub><sup>-</sup>, and reacted with Fe(III) to form Fe(II). Meanwhile, Fe(II) reacted with HSO<sub>5</sub><sup>-</sup> to generate Fe(III) and SO<sub>4</sub><sup>•-</sup>. In addition, •O<sub>2</sub><sup>-</sup> reacted with H<sup>+</sup> ions in TCH solution to form •OOH, and then to produce H<sub>2</sub>O<sub>2</sub>. H<sub>2</sub>O<sub>2</sub> was further converted to •OH and OH<sup>-</sup>, of which OH<sup>-</sup> reacted with h<sup>+</sup> to form •OH. SO<sub>4</sub><sup>•-</sup> could react with H<sub>2</sub>O to produce •OH and SO<sub>4</sub><sup>2-</sup>. •OH reacted with •O<sub>2</sub><sup>-</sup> to form <sup>1</sup>O<sub>2</sub> and OH<sup>-</sup>. Considering that SO<sub>4</sub><sup>•-</sup> radicals easily formed S<sub>2</sub>O<sub>8</sub><sup>2-</sup>, S<sub>2</sub>O<sub>8</sub><sup>2-</sup> reacted with Fe(III) to form Fe(II) and •S<sub>2</sub>O<sub>8</sub><sup>2-</sup>, and reacted with Fe(II) to form Fe(III), SO<sub>4</sub><sup>•-</sup>, and SO<sub>4</sub><sup>2-</sup> [50]. For comparison to the potential value of OH<sup>-</sup>/•OH (1.99 eV), the less positive E<sub>VB</sub> value was not suitable for the reaction between H<sub>2</sub>O and h<sup>+</sup> to generate •OH. These formed SO<sub>4</sub><sup>•-</sup>, •OH, •O<sub>2</sub><sup>-</sup>, and <sup>1</sup>O<sub>2</sub> efficiently attacked the functional groups of TCH species to form intermediates, and even harmless products such as H<sub>2</sub>O and CO<sub>2</sub>.

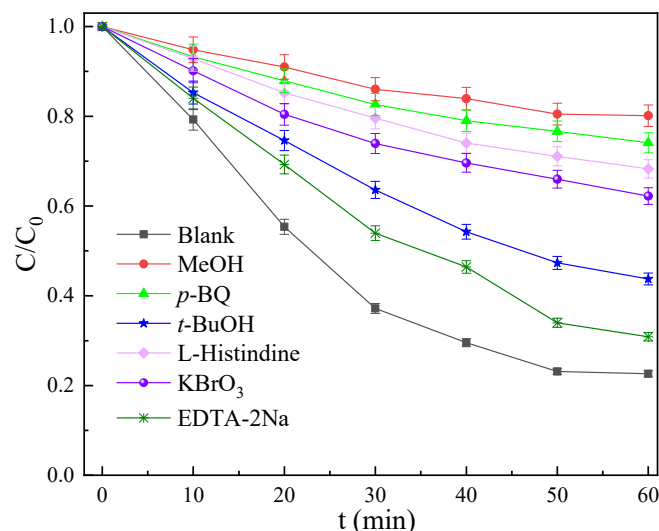


Figure 5. Quenching tests of MgFe<sub>2</sub>/PAN for photo-PMS elimination of TCH.

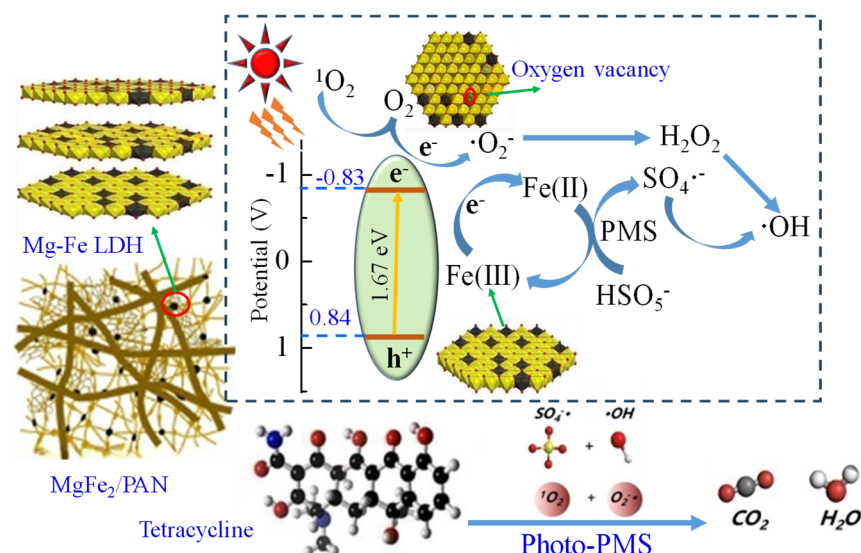


Figure 6. Photo-PMS mechanism of MgFe<sub>2</sub>/PAN composites for TCH elimination.

#### 4. Conclusions

Mg-Fe/PAN nanofibers were fabricated via the hydrothermal route to improve the photo-PMS performance in TCH elimination. In comparison with PAN, Mg(OH)<sub>2</sub>/PAN and Fe(OH)<sub>3</sub>/PAN, MgFe<sub>2</sub>/PAN had the best photo-PMS activity. MgFe<sub>2</sub>/PAN could degrade an 81.31% TCH solution of 80 mg L<sup>-1</sup> within 120 min. On the one hand, the sufficient vacant sites generated from functional groups and lattice defects favored TCH adsorption and photon capture. On the other hand, the photogenerated e<sup>-</sup>/h<sup>+</sup> pairs were efficiently separated and migrated at the tight junction interface between Mg-Fe LDH and PAN nanofibers. Notably, SO<sub>4</sub><sup>•-</sup>, •OH, •O<sub>2</sub><sup>-</sup>, and <sup>1</sup>O<sub>2</sub> played important roles in the photo-PMS process. However, the long-term irradiation induced serious photo-corrosion, changing the valence states of surface compositions. The removal efficiency of MgFe<sub>2</sub>/PAN for 70 mg L<sup>-1</sup> TCH solution declined from 87.23% to 83.39% after five cycles. Hence, future work should focus on the enhancement of the photo-PMS durability of Mg-Fe/PAN composites for wastewater treatment.

**Supplementary Materials:** The following supporting information can be downloaded at: <https://www.mdpi.com/article/10.3390/w16101345/s1>. S1. Characterization. Figure S1. SEM images of MgFe/PAN (A and B), MgFe<sub>2</sub>/PAN (C and D), MgFe<sub>3</sub>/PAN (E and F), and Mg<sub>2</sub>Fe/PAN (G and

H). Figure S2. Elemental mapping images and EDX pattern of MgFe<sub>2</sub>/PAN. Figure S3. UV-vis DRS curves (A), plots of  $(h\nu)$  versus  $(\alpha h\nu)^{1/2}$ , Mott-Schottky curves (C), and electrochemical impedance spectra (D) of MgFe/PAN with various Mg/Fe molar ratios. Figure S4. FT-IR spectra of PAN nanofibers. Figure S5. Zeta potential curve of MgFe<sub>2</sub>/PAN. Figure S6. Effect of TCH concentration on the photo-PMS kinetics of MgFe<sub>2</sub>/PAN for TCH removal. Figure S7. Effect of pH on the photo-PMS kinetics of MgFe<sub>2</sub>/PAN for TCH removal. Figure S8. Mg 1s (A), Fe 2p (B), C 1s (C), O 1s (D), and N 1s (E) XPS spectra of used MgFe<sub>2</sub>/PAN. Figure S9. SEM images of used MgFe<sub>2</sub>/PAN. Table S1. band gap energies and electronic properties of PAN and Mg-Fe/PAN composites. Table S2. Degradation capacities of MgFe<sub>2</sub>/PAN and reported materials for TCH elimination. References [51–58] are cited in the Supplementary Materials.

**Author Contributions:** Conceptualization, M.L.; Methodology, H.P.; Software, X.Z.; Validation, X.Z.; Formal analysis, B.Y.; Investigation, B.Y.; Data curation, M.L.; Writing—original draft, H.P.; Writing—review & editing, X.Z.; Supervision, X.Z. All authors have read and agreed to the published version of the manuscript.

**Funding:** This research received no external funding.

**Data Availability Statement:** Data are contained within the article and Supplementary Materials.

**Conflicts of Interest:** The authors declare no conflict of interest.

## References

1. Biswal, B.K.; Balasubramanian, R. Adsorptive removal of sulfonamides, tetracyclines and quinolones from wastewater and water using carbon-based materials: Recent developments and future directions. *J. Clean. Prod.* **2022**, *349*, 131421. [[CrossRef](#)]
2. Sugitha, S.K.J.; Venkatesan, R.; Latha, R.G.; Vetcher, A.A.; Al-Asbahi, B.A.; Kim, S.C. A study on the antibacterial, antispasmodic, antipyretic, and anti-inflammatory activity of ZnO nanoparticles using leaf extract from *Jasminum sambac* (L. Aiton). *Molecules* **2024**, *29*, 1464. [[CrossRef](#)] [[PubMed](#)]
3. Sivaprakash, P.; Venkatesan, R.; Muthu, S.E.; Hatshan, M.R.; Vetcher, A.A.; Kim, S.-C.; Kim, I. Effect of different etching times on the structural, morphological, electrical, and antimicrobial properties of mesoporous silicon. *Heliyon* **2023**, *9*, e23105. [[CrossRef](#)] [[PubMed](#)]
4. Pulicharla, R.; Hegde, K.; Brar, S.K.; Surampalli, R.Y. Tetracyclines metal complexation: Significance and fate of mutual existence in the environment. *Environ. Poll.* **2017**, *221*, 1–14. [[CrossRef](#)] [[PubMed](#)]
5. Li, J.; Qin, Y.; Zhao, C.; Zhang, Z.; Zhou, Z. Tetracycline antibiotics: Potential anticancer drugs. *Eur. J. Pharmacol.* **2023**, *956*, 175949. [[CrossRef](#)] [[PubMed](#)]
6. Ajiboye, T.O.; Sawunyama, L.; Ravele, M.P.; Rasheed-Adeleke, A.A.; Seheri, N.H.; Onwudiwe, D.C.; Mhlanga, S.D. Synthesis approaches to ceramic membranes, their composites, and application in the removal of tetracycline from water. *Environ. Adv.* **2023**, *12*, 100371. [[CrossRef](#)]
7. Filho, F.G.N.; Filho, E.C.S.; Osajima, J.A.; de Melo Alves, A.P.; Fonseca, M.G. Adsorption of tetracycline using chi-tosan–alginate–bentonite composites. *Appl. Clay Sci.* **2023**, *239*, 106952. [[CrossRef](#)]
8. Varadharajan, V.; Senthilkumar, D.S.; Senthilkumar, K.; Sundramurthy, V.P.; Manikandan, R.; Senthilarasan, H.; Ganesan, H.; Kesavamoorthy, I.; Ramasamy, A. Process modeling and toxicological evaluation of adsorption of tetracycline onto the magnet-ized cotton dust biochar. *J. Water Process Eng.* **2022**, *49*, 103046. [[CrossRef](#)]
9. Wang, J.; Yi, X.; Xu, X.; Ji, H.; Alanazi, A.M.; Wang, C.; Zhao, C.; Kaneti, Y.V.; Wang, P.; Liu, W.; et al. Eliminating tetracycline antibiotics matrix via photoactivated sulfate radical-based advanced oxidation process over the immobilized MIL-88A: Batch and continuous experiments. *Chem. Eng. J.* **2022**, *431*, 133213. [[CrossRef](#)]
10. Aryee, A.A.; Ma, Y.; Wang, J.; Han, R.; Qu, L. A magnetic biomass/MOF composite as a functional material for the oxidative removal of tetracycline: Degradation mechanism and toxicity study. *J. Environ. Chem. Eng.* **2023**, *11*, 110663. [[CrossRef](#)]
11. Chen, X.; Zhu, Y.; Chen, J.; Yan, S.; Xie, S. Multi-omic profiling of a novel activated sludge strain *Sphingobacterium* sp. WM1 reveals the mechanism of tetracycline biodegradation and its merits of potential application. *Water Res.* **2023**, *243*, 120397. [[CrossRef](#)]
12. Wang, L.; Ye, Y.; Zeng, Z.; Wang, Y.; Han, M. Efficient removal of tetracycline in water by a Fe<sub>3</sub>O<sub>4</sub>-mediated persulfate activation and biodegradation coupled system: Performance, validation, and mechanism. *J. Water Process Eng.* **2023**, *53*, 103718. [[CrossRef](#)]
13. Yang, S.; Feng, Y.; Gao, D.; Wang, X.; Suo, N.; Yu, Y.; Zhang, S. Electrocatalysis degradation of tetracycline in a three-dimensional aeration electrocatalysis reactor (3D-AER) with a flotation-tailings particle electrode (FPE): Physicochemical properties, influencing factors and the degradation mechanism. *J. Hazard. Mater.* **2020**, *407*, 124361. [[CrossRef](#)]
14. Shi, C.; Yu, S.; Wang, L.; Zhang, X.; Lin, X.; Li, C. Degradation of tetracycline/oxytetracycline by electrospun aligned polyacrylonitrile-based carbon nanofibers as anodic electrocatalysis microfiltration membrane. *J. Environ. Chem. Eng.* **2021**, *9*, 106540. [[CrossRef](#)]

15. Swedha, M.; Balasurya, S.; Syed, A.; Das, A.; Khan, S.S. Continuous photocatalysis via Z-scheme based nanocatalyst system for environmental remediation of pharmaceutically active compound: Modification, reaction site, defect engineering and challenges on the nanocatalyst. *J. Mol. Liq.* **2022**, *353*, 118745. [[CrossRef](#)]
16. Haleem, A.; Pan, J.-M.; Shah, A.; Hussain, H.; He, W.-D. A systematic review on new advancement and assessment of emerging polymeric cryogels for environmental sustainability and energy production. *Sep. Purif. Technol.* **2023**, *316*, 123678. [[CrossRef](#)]
17. Amaly, N.; EL-Moghazy, A.Y.; Nitin, N.; Sun, G.; Pandey, P.K. Design, preparation, and application of novel multilayer metal-polyphenol composite on macroporous framework melamine foam for effective filtration removal of tetracycline in fluidic systems. *Sep. Purif. Technol.* **2023**, *321*, 124238. [[CrossRef](#)]
18. Xiong, H.-Q.; Bao, H.-R.; Long, F.; Du, Y.-Y.; Qu, J.-Z.; Luan, Z.-X.; Sun, X.-L. From lab to nature: Overcoming challenges in applying in-situ photocatalysis to water bodies. *J. Environ. Chem. Eng.* **2024**, *12*, 112656. [[CrossRef](#)]
19. Zhu, C.; Wang, Y.; Qiu, L.; Yang, W.; Yu, Y.; Li, J.; Liu, Y. Z-scheme NiFe LDH/Bi<sub>4</sub>O<sub>5</sub>I<sub>2</sub> heterojunction for photo-Fenton oxidation of tetracycline. *J. Alloys Compd.* **2023**, *944*, 169124. [[CrossRef](#)]
20. Fazli, A.; Brigante, M.; Khataee, A.; Mailhot, G. Fe<sub>2.5</sub>Co<sub>0.3</sub>Zn<sub>0.2</sub>O<sub>4</sub>/CuCr-LDH as a visible-light-responsive photocatalyst for the degradation of caffeine, bisphenol A, and simazine in pure water and real wastewater under photo-Fenton-like degradation process. *Chemosphere* **2022**, *291*, 132920. [[CrossRef](#)]
21. Cao, Y.; Guo, Q.; Liang, M.; Sun, W. Sb(III) and Sb(V) removal from water by a hydroxyl-intercalated, mechanochemically synthesized Mg-Fe-LDH. *Appl. Clay Sci.* **2020**, *196*, 105766. [[CrossRef](#)]
22. Hudcová, B.; Fein, J.B.; Tsang, D.C.W.; Komárek, M. Mg-Fe LDH-coated biochars for metal(loid) removal: Surface complexation modeling and structural change investigations. *Chem. Eng. J.* **2022**, *432*, 134360. [[CrossRef](#)]
23. Ji, Y.; Song, Z.; Xu, Y.; Zhang, Y. Cu-Fe LDHs/Bi<sub>2</sub>WO<sub>6</sub> composite for superior photo-Fenton Rhodamine B removal through combination of photogenerated electrons and multivalent bimetal redox for accelerating Fe<sup>3+</sup>/Fe<sup>2+</sup> cycles. *J. Alloys Compd.* **2022**, *925*, 166655. [[CrossRef](#)]
24. Dong, Z.; Du, X.; Zhu, X.; Huang, E.; An, Y. Regulate the behaviors of photo-generated carriers in CuFe-LDH/TiO<sub>2</sub> based on positive bias voltage to enhance the capability of photo-Fenton on nitrobenzene degradation. *Appl. Surf. Sci.* **2022**, *602*, 154312. [[CrossRef](#)]
25. Yang, L.; Li, L.; Liu, Z.; Lai, C.; Yang, X.; Shi, X.; Liu, S.; Zhang, M.; Fu, Y.; Zhou, X.; et al. Degradation of tetracycline by FeNi-LDH/Ti<sub>3</sub>C<sub>2</sub> photo-Fenton system in water: From performance to mechanism. *Chemosphere* **2022**, *294*, 133736. [[CrossRef](#)] [[PubMed](#)]
26. Costa-Serge, N.d.M.; Gonçalves, R.G.L.; Ramirez-Ubillus, M.A.; Li, C.; Hammer, P.; Chiron, S.; Nogueira, F.P. Effect of the interlamellar anion on CuMgFe-LDH in solar photo-Fenton and Fenton-like degradation of the anticancer drug 5-fluorouracil. *Appl. Catal. B Environ.* **2022**, *315*, 121537. [[CrossRef](#)]
27. Shao, B.; Liu, Z.; Tang, L.; Liang, Q.; He, Q.; Wu, T.; Pan, Y.; Cheng, M.; Liu, Y.; Tan, X.; et al. Construction of Bi<sub>2</sub>WO<sub>6</sub>/CoAl-LDHs S-scheme heterojunction with efficient photo-Fenton-like catalytic performance: Experimental and theoretical studies. *Chemosphere* **2022**, *291*, 133001. [[CrossRef](#)]
28. Li, X.; Meng, Y.; Li, J.; Zhang, L.; Xie, B.; Ni, Z.; Xia, S. The performance and mechanism of persulfate activation boosted MoO<sub>2</sub>@LDHs Z-scheme heterojunction for efficient photocatalytic degradation of tetracycline. *J. Environ. Chem. Eng.* **2023**, *11*, 110257. [[CrossRef](#)]
29. Zhang, X.; Zong, Y.; Xu, L.; Mao, Y.; Wu, D. Enhanced abiotic integrated polyphenol-Maillard humification by Mg/Fe layered double hydroxide (LDH): Role of Fe(III)-polyphenol complexation. *Chem. Eng. J.* **2021**, *425*, 130521. [[CrossRef](#)]
30. Gonçalves, R.G.L.; Mendes, H.M.; Bastos, S.L.; D'Agostino, L.C.; Tronto, J.; Pulcinelli, S.H.; Santilli, C.V.; Neto, J.L. Fenton-like degradation of methylene blue using Mg/Fe and MnMg/Fe layered double hydroxides as reusable catalysts. *Appl. Clay Sci.* **2020**, *187*, 105477. [[CrossRef](#)]
31. Pelalak, R.; Hassani, A.; Heidari, Z.; Zhou, M. State-of-the-art recent applications of layered double hydroxides (LDHs) material in Fenton-based oxidation processes for water and wastewater treatment. *Chem. Eng. J.* **2023**, *474*, 145511. [[CrossRef](#)]
32. Khan, A.A.; Tahir, M.; Khan, N. LDH-based nanomaterials for photocatalytic applications: A comprehensive review on the role of bi/trivalent cations, anions, morphology, defect engineering, memory effect, and heterojunction formation. *J. Energy Chem.* **2023**, *84*, 242–276. [[CrossRef](#)]
33. Haleem, A.; Shafiq, A.; Chen, S.Q.; Nazar, M. A comprehensive review on adsorption, photocatalytic and chemical degradation of dyes and nitro-compounds over different kinds of porous and composite materials. *Molecules* **2023**, *28*, 1081. [[CrossRef](#)] [[PubMed](#)]
34. Li, S.; Long, K.; Sun, X.; Yuan, H.; Li, W. Activities in photocatalytic hydrogen evolution of In<sub>2</sub>O<sub>3</sub>/In<sub>2</sub>S<sub>3</sub> heterostructure and In<sub>2</sub>O<sub>3</sub>/In<sub>2</sub>S<sub>3</sub>@PAN nanofibers. *Ceram. Int.* **2023**, *49*, 24093–24099. [[CrossRef](#)]
35. Zhang, Q.; Li, G.; Bai, J.; He, R.; Li, C. Enhanced photocatalytic activities of CdS-BiOCl/PAN composites towards photocatalytic hydrogen evolution. *Mater. Res. Bull.* **2019**, *117*, 9–17. [[CrossRef](#)]
36. Mao, Y.; Lin, L.; Chen, Y.; Yang, M.; Zhang, L.; Dai, X.; He, Q.; Jiang, Y.; Chen, H.; Liao, J.; et al. Preparation of site-specific Z-scheme g-C<sub>3</sub>N<sub>4</sub>/PAN/PANI@LaFeO<sub>3</sub> cable nanofiber membranes by coaxial electrospinning: Enhancing filtration and photocatalysis performance. *Chemosphere* **2023**, *328*, 138553. [[CrossRef](#)] [[PubMed](#)]
37. Ding, D.; Li, Z.; Yu, S.; Yang, B.; Yin, Y.; Zan, L.; Myung, N.V. Piezo-photocatalytic flexible PAN/TiO<sub>2</sub> composite nanofibers for environmental remediation. *Sci. Total Environ.* **2022**, *824*, 153790. [[CrossRef](#)]

38. Chen, Y.; Zhang, H.; Liu, K.; Zhu, X.; Yuan, H.; Wang, C. Photocatalytic activities of Bi<sub>2</sub>O<sub>2</sub>CO<sub>3</sub>/g-C<sub>3</sub>N<sub>4</sub>@PAN nanofibers in hydrogen production. *Appl. Surf. Sci.* **2022**, *599*, 154013. [[CrossRef](#)]
39. Tian, J.; Zhang, Y.; Qian, F.; Cao, M.; Cheng, Y.; Li, J.; Tian, M.; Li, W.; Wang, L. The design of novel swash plate photocatalytic reactor with PAN/BiInOCl membrane photocatalyst for excellent RhB degradation. *J. Alloys Compd.* **2023**, *968*, 171894. [[CrossRef](#)]
40. Teng, P.; Zhu, J.; Li, Z.; Li, K.; Copner, N.; Gao, S.; Zhao, E.; Zhu, X.; Liu, Z.; Tian, F.; et al. Flexible PAN-Bi<sub>2</sub>O<sub>2</sub>CO<sub>3</sub>-BiOI heterojunction nanofiber and the photocatalytic degradation property. *Opt. Mater.* **2022**, *134*, 112935. [[CrossRef](#)]
41. Daulbayev, C.; Sultanov, F.; Korobeinyk, A.V.; Yeleuov, M.; Azat, S.; Bakbolat, B.; Umirzakov, A.; Mansurov, Z. Bio-waste-derived few-layered graphene/SrTiO<sub>3</sub>/PAN as efficient photocatalytic system for water splitting. *Appl. Surf. Sci.* **2021**, *549*, 149176. [[CrossRef](#)]
42. Chen, G.; Wong, N.H.; Sunarso, J.; Wang, Y.; Liu, Z.; Chen, D.; Wang, D.; Dai, G. Flexible Bi<sub>2</sub>MoO<sub>6</sub>/S-C<sub>3</sub>N<sub>4</sub>/PAN heterojunction nanofibers made from electrospinning and solvothermal route for boosting visible-light photocatalytic performance. *Appl. Surf. Sci.* **2023**, *612*, 155893. [[CrossRef](#)]
43. Liu, Z.; Ren, X.; Duan, X.; Sarmah, A.K.; Zhao, X. Remediation of environmentally persistent organic pollutants (POPs) by persulfates oxidation system (PS): A review. *Sci. Total Environ.* **2023**, *863*, 160818. [[CrossRef](#)]
44. Ghamkhari, A.; Mohamadi, L.; Kazemzadeh, S.; Zafar, M.N.; Rahdar, A.; Khaksefidi, R. Synthesis and characterization of poly(styrene-block-acrylic acid) diblock copolymer modified magnetite nanocomposite for efficient removal of penicillin G. *Compos. Part B Eng.* **2019**, *182*, 107643. [[CrossRef](#)]
45. Greczynski, G.; Hultman, L. X-ray photoelectron spectroscopy: Towards reliable binding energy referencing. *Prog. Mater. Sci.* **2019**, *107*, 100591. [[CrossRef](#)]
46. Ayiania, M.; Smith, M.; Hensley, A.J.R.; Scudiero, L.; McEwen, J.S.; Garcia-Perez, M. Deconvoluting the XPS spectra for ni-trogen-doped chars: An analysis from first principles. *Carbon* **2020**, *162*, 528–544. [[CrossRef](#)]
47. Nayak, S.; Swain, G.; Parida, K. Enhanced photocatalytic activities of RhB degradation and H<sub>2</sub> evolution from in situ formation of the electrostatic heterostructure MoS<sub>2</sub>/NiFe LDH nanocomposite through the Z-scheme mechanism via p-n heterojunctions. *ACS Appl. Mater. Interfaces* **2019**, *11*, 20923–20942. [[CrossRef](#)]
48. Lian, Z.; Wu, T.; Zhang, X.; Cai, S.; Xiong, Y.; Yang, R. Synergistic degradation of tetracycline from Mo<sub>2</sub>C/MoO<sub>x</sub> films mediated peroxymonosulfate activation and visible-light triggered photocatalysis. *Chem. Eng. J.* **2023**, *469*, 143774. [[CrossRef](#)]
49. Wang, Y.; Liu, C.; Wang, C.; Hu, Q.; Ding, L. 0D/3D NiCo<sub>2</sub>O<sub>4</sub>/defected UiO-66 catalysts for enhanced degradation of tetracycline in peroxymonosulfate/simulated sunlight systems: Degradation mechanisms and pathways. *Chemosphere* **2022**, *299*, 134322. [[CrossRef](#)]
50. Wang, R.; Yu, Y.; Zhang, R.; Ren, X.; Guo, W. Vacancy-rich structure inducing efficient persulfate activation for tetracycline degradation over Ni-Fe layered double hydroxide nanosheets. *Sep. Purif. Technol.* **2022**, *289*, 120663. [[CrossRef](#)]
51. Zheng, J.; Fan, C.; Li, X.; Yang, Q.; Wang, D.; Duan, A.; Pan, S.; Zhang, B.; Ding, J.; Rong, S.; et al. Effective mineralization and detoxification of tetracycline hydrochloride enabled by oxygen vacancies in g-C<sub>3</sub>N<sub>4</sub>/LDH composites. *Sep. Purif. Technol.* **2023**, *305*, 122554. [[CrossRef](#)]
52. Zhang, X.; Duan, Y.; Li, Y.; Dong, W.; Wu, S.; Duan, Q. Porphyrin-TiO<sub>2</sub> encapsulated ZIF-8/PAN-derived porous carbon nanofiber ternary photocatalyst with enhanced photodegradation efficiency through synergistic effect. *Vacuum* **2023**, *218*, 112673. [[CrossRef](#)]
53. Luo, Y.; Shi, G.; Yu, S.; Liu, Z.; Yin, J.; Xue, M.; Sun, Q.; Shen, F.; Li, X.; Yin, Z.; et al. Novel MIL-88B(Fe)/ZnTi-LDH high-low junctions for adsorption and photodegradation of tetracycline: Characteristics, performance, and mechanisms. *Chem. Eng. J.* **2023**, *473*, 145198. [[CrossRef](#)]
54. Sun, Y.; Wang, L.; Wang, T.; Liu, X.; Xu, T.; Wei, M.; Yang, L.; Li, C. Improved photocatalytic activity of Ni<sub>2</sub>P/NiCo-LDH composites via a Co-P bond charge transfer channel to degrade tetracycline under visible light. *J. Alloys Compd.* **2021**, *852*, 156963. [[CrossRef](#)]
55. Devi, S.K.; Thirumal, V.; Balamurugan, A.; Avula, B.; Pongiya, U.D.; Kim, J.; Surya, C. Photocatalytic degradation of tetracycline over ternary NiCoMn-LDH under visible light illumination. *ACS Mater. Lett.* **2023**, *350*, 134910. [[CrossRef](#)]
56. Wang, T.; Yang, Y.; Deng, Q.; Zhang, X.; Xiong, L.; Tang, Z.; Li, P.; Yin, N.; Sun, A.; Chen, D.; et al. In-situ construction of 3D marigold-like CoAl-LDH/Ti<sub>3</sub>C<sub>2</sub> heterosystem collaborating with 2D/2D interface for efficient photodegradation of multiple antibiotics. *Appl. Surf. Sci.* **2021**, *569*, 151084. [[CrossRef](#)]
57. Shi, H.; Yang, X.; Zuo, Y.; Yang, H.; Zhang, R.; Zhang, Y.; Fan, Y.; Du, X.; Jiang, L. Construction of Fe<sub>3</sub>O<sub>4</sub>/FeP binary composite catalyst for degradation of tetracycline in wastewater. *Int. J. Electrochem. Soc.* **2021**, *16*, 210314. [[CrossRef](#)]
58. Wang, Z.; Lai, C.; Qin, L.; Fu, Y.; He, J.; Huang, D.; Li, B.; Zhang, M.; Liu, S.; Li, L.; et al. ZIF-8-modified MnFe<sub>2</sub>O<sub>4</sub> with high crystallinity and superior photo-Fenton catalytic activity by Zn-O-Fe structure for TC degradation. *Chem. Eng. J.* **2020**, *392*, 124851. [[CrossRef](#)]

**Disclaimer/Publisher's Note:** The statements, opinions and data contained in all publications are solely those of the individual author(s) and contributor(s) and not of MDPI and/or the editor(s). MDPI and/or the editor(s) disclaim responsibility for any injury to people or property resulting from any ideas, methods, instructions or products referred to in the content.